EFFECTS OF SEDIMENT SHAPE AND ANGULARITY IN OSCILLATORY TURBULENT FLOWS

Umberto Ciri
Dept. of Mechanical Engineering
University of Puerto Rico at Mayagüez
PO Box 9000, Mayagüez, PR 00680, US
umberto.ciri@upr.edu

Tzunami Santiago-Pagán
Dept. of Mechanical Engineering
University of Puerto Rico at Mayagüez
PO Box 9000, Mayagüez, PR 00680, US
tzunami.santiago@upr.edu

Sylvia Rodríguez-Abudo
Dept. of Engineering Sciences and Materials
University of Puerto Rico at Mayagüez
PO Box 9000, Mayagüez, PR 00680, US
rodriguez.abudo@upr.edu

Stefano Leonardi
Dept. of Mechanical Engineering
The University of Texas at Dallas
800 W Campbell Rd, Richardson, TX 75252 US
stefano.leonardi@utdallas.edu

ABSTRACT

Direct numerical simulations of oscillatory turbulent flows over different rough walls have been performed. The rough walls consist of three sediment beds with different particles each, respectively disks, ellipses, and pyramids. These sediment shapes are representative of seabeds in tropical coastal areas and are selected to assess the hydrodynamic effect of sediment shape by comparing relatively round particles (ellipses) with very angular sediments (pyramids) and sediments with sharp edges (disks). The beds are represented with the immersed boundary method. Bulk flow statistics, such as the bed drag, tend to scale fairly well with classic single-parameter roughness characterization, such as the equivalent roughness length. Nevertheless, additional features, such as roughness shape or angularity, seem to have a significant effect when considering higher-order flow statistics, including not only the turbulence flow field, but also ensemble-averaged velocity statistics, such as the boundary layer thickness and the phase lead. The results suggest that for scenarios that depart from ‘spherical-sand’ roughness predominant in the literature, more than one geometrical bed parameter may be required to capture the effect of sediment shape and angularity.

INTRODUCTION

Seabed hydrodynamics in littoral areas is characterized by oscillatory motion in the bottom boundary layer. The oscillatory bottom boundary layer affects sediment erosion, transport and deposition patterns, as well as the fate of nutrients dispersed in the water. Thus, the oscillatory bottom boundary layer is a key component in the seabed ecosystem dynamics and has been widely studied. Despite significant research progress made over the years, a complete understanding of this flow is still lacking.

A critical challenge is that the flow in the boundary layer tends to be turbulent and the seabed is rough. The seabed is typically made of particles (sediments) that, depending on the location, have not only different sizes, but also varying shapes and angularities. Building upon uni-directional (rather than oscillatory) rough boundary layer literature, roughness size can arguably be assumed sufficient to mainly characterize the bed surface, at least to a first approximation. Dimensional analysis then shows that, for a free stream oscillating with velocity amplitude U_0 and frequency ω, flow behaviour is a function of the Reynolds number and the ratio of the oscillation amplitude to the roughness size (Jonsson, 1966). The Reynolds number is variably defined in the literature as $Re = U_0 a/\nu$, where $a = U_0/\omega$ is the oscillation amplitude (i.e., the distance travelled by a particle over a period) and ν is the kinematic viscosity of the fluid), or $Re_\delta = U_0\delta/\nu = \sqrt{2Re}$, where $\delta = \sqrt{2\nu/\omega}$ is the Stokes layer depth, a measure of the boundary layer thickness in the (sinusoidally) oscillating laminar flow over a smooth flat plate (the classical Stokes' second problem, see e.g. Batchelor, 1967).

Early studies have thus attempted at a flow characterization in the parameter space comprised of Reynolds number Re and, following classic rough-wall turbulence, the ratio a/k_s, where k_s is Nikuradse's equivalent sand-grain roughness (Jonsson & Carlsen, 1976; Sleath, 1987; Jensen *et al.*, 1989). Even when the Reynolds number is not too large and the flow is laminar, bed roughness causes departures from the laminar Stokes' flat-plate solution with the appearance of secondary velocity maxima over a period and phase-coherent (in the sense of a triple decomposition following Hussain & Reynolds, 1970) vertical Reynolds stresses (Keiller & Sleath, 1976). As the Reynolds number increases and the flow becomes fully turbulent, a number of studies have highlighted further modifications in the flow structure compared to the laminar or turbulent smooth wall reference that include, for the mean flow, the thickening of the boundary layer with a/k_s and an increase of the phase shift across the boundary layer (Dixen *et al.*, 2008; Ghodke & Apte, 2016). At the same time, the turbulent flow field exhibits increased fluctuations and energy fluxes between the turbulent (random) and phase-coherent components and a general tendency toward isotropy (Fornarelli & Vittori, 2009; Ghodke & Apte, 2016; Ciri *et al.*, 2023).

In recent years, progress in numerical techniques and computing power has provided flow information at a level of detail that was previously difficult to obtain experimentally. For instance, direct numerical simulations (DNS) based on the immersed boundary method and parallel computing have explored mean flow patterns and coherent structures around single sediments in the bed and analyzed generation mechanisms and dynamics of lift and drag forces on individual particles (Mazzuoli & Vittori, 2016; Mazzuoli & Uhlmann, 2017; Ghodke & Apte, 2018*a*,*b*). While results have emphasized that details of the flow around the sediments have an important impact on the overall bed hydrodynamics, nevertheless these studies have been limited to spherical particles. Likewise, most of the previous work in the literature has analyzed spherical particles or other relatively rounded shapes, which are representative of common non-cohesive silica sands (see e.g. Dixen *et al.*, 2008; Chan-Braun *et al.*, 2011; Mazzuoli & Uhlmann, 2017; O'Donoghue *et al.*, 2021; Dunbar *et al.*, 2023*a*). In contrast, less attention has been devoted to other sediment shapes that are common, for example, in tropical areas and include fairly angular sediments and sharp edges. As particle geometry and spatial distribution are likely to have an impact on the bottom hydrodynamics, in this work, we consider beds with particles in the shapes of either ellipses, disks, or pyramids. The aim is to obtain a first assessment of changes in hydrodynamics due to particle shape by comparing relatively round sediments (such as ellipses) with very angular sediments (pyramids) and sediments with sharp edges (disks). The study is conducted using direct numerical simulations coupled with an immersed boundary method to treat the bed. The oscillation is imposed through a sinusoidal velocity boundary condition on the rough bed, which mimics the shear-driven flow commonly observed in oscillating tray rigs experiments. The numerical methodology is described in the next section, followed by the analysis of the results and concluding remarks.

NUMERICAL METHODOLOGY

The incompressible non-dimensional continuity and Navier-Stokes equations are taken as the governing equations:

$$\frac{\partial U_i}{\partial x_i} = 0; \quad \frac{\partial U_i}{\partial t} + \frac{\partial U_i U_j}{\partial x_j} = -\frac{\partial P}{\partial x_i} + \frac{1}{Re}\frac{\partial U_i}{\partial x_j^2} \qquad (1)$$

where U_i is the velocity component in direction x_i ($i = 1,2,3$ or x,y,z for streamwise, spanwise and bed-normal direction, respectively) and P is the pressure. The Reynolds number $Re = U_0 a/\nu$ is defined with the oscillation amplitudes U_0 and $a = U_0/\omega$, where ω is the oscillation frequency, and ν the fluid kinematic viscosity.

The numerical method for solving the governing equations is described in Orlandi (2000). The staggered central second-order energy-conserving finite-difference scheme is used to discretize the spatial derivatives in an orthogonal coordinate system. A hybrid low-storage third-order Runge-Kutta scheme, with linear terms treated implicitly and convective terms treated explicitly, is used to advance the equation in time. The matrix resulting from the implicit terms is inverted with an approximate factorization technique. The fractional-step method is used to treat the pressure. The momentum equations are advanced with the pressure at the previous step, yielding an intermediate non-solenoidal velocity field. A scalar quantity is used to project the non-solenoidal field onto a solenoidal one. The substrate textures are treated with the immersed boundary method (IBM) presented in detail in Orlandi & Leonardi (2006). The immersed boundary method is also used to apply the shear-driven forcing as a boundary condition on the velocity at the bed.

Simulations are performed for an open channel with different rough beds on the lower boundary of the computational domain (figure 1). The bed geometries have been reconstructed from experiments carried out in an oscillatory boundary layer facility (Vargas-Martinez & Rodríguez-Abudo, 2024). Therein, particles with different shapes (specifically either disks, ellipses or pyramids) were disposed on the oscillating tray. The bed geometry was reconstructed by processing images taken during the experimental runs in the streamwise (x) and wall-normal (z) plane: the crest profile was decomposed into its Fourier modes and replicated in the spanwise direction to recreate a three-dimensional bed height $k(x,y)$. The resulting geometry is shown in figure 1 for the three cases, which are denoted with the original sediment shapes as disks, ellipses and pyramids. The IBM does not replicate the individual bed sediments, but rather the collective distribution $k(x,y)$ shown in the figure, and the bed is rigid (there is no relative movement between the sediments). The aim here is to obtain a first assessment of changes in the hydrodynamics due to particle shape by comparing relatively round sediments (such as ellipses) with very angular sediments (pyramids) and sediments with sharp edges (disks). As shown in table 1, the disk and ellipse geometries have fairly similar bed heights, while the pyramid bed is rougher.

Table 1. Statistics of the bed geometries, normalized by the Stokes' length $\delta = \sqrt{2\nu/\omega}$: mean height k_{mean}, max height $k_{\max}$, root mean square height k_{rms} and skewness Sk.

Geometry	k_{mean}/δ	$k_{\max}/\delta$	k_{rms}/δ	Sk
Disks	0.964	2.048	0.161	0.238
Ellipses	0.942	2.089	0.159	0.169
Pyramids	2.003	4.096	0.313	0.047

The computational domain is about $150\delta \times 150\delta \times 50\delta$ in the streamwise, spanwise and bed-normal directions (x, y and z, respectively), where $\delta = \sqrt{2\nu/\omega}$ is the Stokes' boundary layer thickness. The mesh consists of $800 \times 720 \times 380$ grid-points. The mesh is uniform in the x and y directions, while stretching is applied in the bed-normal direction to increase the resolution near the wall. The resulting mesh spacing Δz is such that about 15 grid-points per Stokes' length are present above the bed.

The boundary conditions are periodic in the x and y directions, and free-slip is applied at the top boundary of the domain. At the bed, a sinusoidal oscillation $U_0 \sin \omega t$ is applied through the immersed boundary method. As discussed in our previous work (Ciri *et al.*, 2024), this approach represents well the shear-driven forcing typical of oscillatory tray rigs, as the apparatus of the experimental reference, from which the bed geometry was taken. The parameters of the oscillations are such that the Reynolds number is $Re = U_0 a/\nu \approx 280{,}000$ (equivalently $Re_\delta \approx 750$), which is in (or at least approaching) the fully turbulent regime (Jensen *et al.*, 1989).

After the initialization, simulations were run $N = 8$ cycles to compute statistics. Turbulent statistics are computed using the triple decomposition (Hussain & Reynolds, 1970) with an ensemble average (denoted with angle brackets) defined by corresponding phases throughout a cycle (a total of 24 phases per cycle are used).

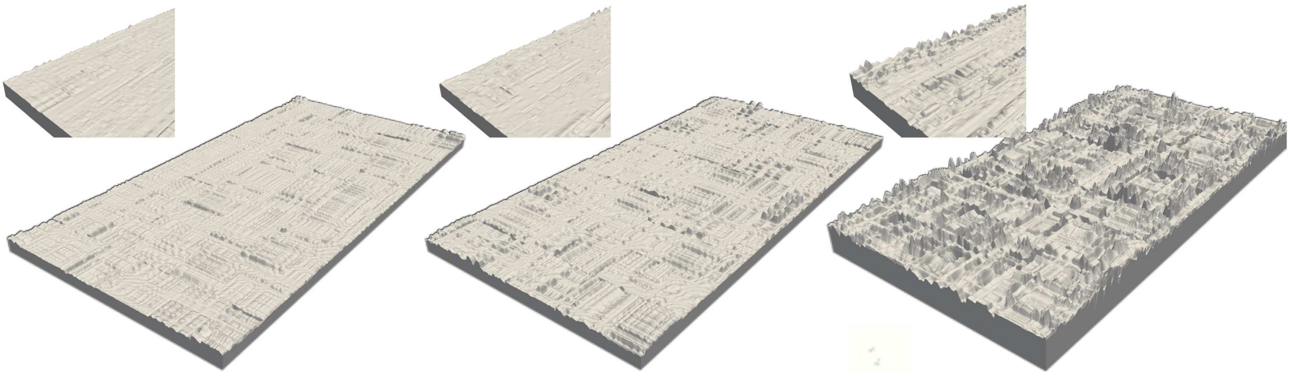

Figure 1. Visualization of the bed geometries from different sediment shapes. From left to right, disks, ellipses and pyramids. The inset at the top right of each case shows a zoom-in of the bed.

RESULTS

Consistent with the analogous unidirectional turbulent boundary-layer case, bed roughness primarily causes an increase in the bottom friction throughout the oscillation. Figure 2*a* shows the friction coefficient $C_f = 2\tau/\rho U_0^2$ as a function of time for half a cycle (the other half is symmetric). The friction coefficient is here defined with the total bed drag, i.e. τ is the sum of the shear and form drag components over the whole bed and is computed from the integral momentum balance (see Arenas *et al.*, 2019, for a derivation). For comparison, the figure also includes the smooth-wall counterparts for the (turbulent) oscillatory flow at the same Reynolds number ($Re = 280,000$, solid line) and the Stokes' solution (dashed line) for the laminar case:

$$C_f = \frac{2}{\sqrt{Re}} \sin(\omega t + \pi/4)\,. \tag{2}$$

The drag scales to a very good approximation with the roughness size (cf. Table 1) as the bed made of ellipses and disks show similar maximum value and temporal behavior, while the pyramid case leads to much larger drag increase.

A key parameter of the stress temporal evolution is the phase shift $\Delta\Phi$ between the maxima in the velocity and shear stress signals (see definition in the inset of figure 2*b*). The shear-velocity phase shift affects the sign of bottom momentum fluxes and is needed in many sediment transport models. For a smooth wall, the stress leads the velocity by $\Delta\Phi = \pi/4 = 45^\circ$deg (see equation 2) in laminar flow, while in the fully turbulent regime the phase lead is reduced to about 10° degrees (Jensen *et al.*, 1989). At intermediate Reynolds number, the behaviour of the phase shift is not trivial, as recently analyzed in detail by Mier *et al.* (2021) and Fytanidis *et al.* (2021). The phase shift initially decreases and turns negative (i.e., stress lagging the velocity) before settling to the 10-degree fully turbulent phase lead. This is due to the fact that, as transition occurs, turbulence initially develops during the deceleration stages of the cycle ($0.25 < t/T < 0.5$ or $\pi/2 < \Phi < \pi$, in terms of phase $\Phi = \omega t$). The turbulence activity leads to a local increase of the bed shear stress and the gradual appearance of a second maximum during the deceleration phases in the bed waveform that is not longer purely sinusoidal as in equation (2). As the flow approaches the fully developed regime, turbulence intensity increases and the secondary "turbulent maximum" in the deceleration phases takes over the "laminar maximum," causing the transient shift from phase lead to phase lag (the velocity peak being fixed at $t = T/4$ or $\Phi = \pi/2$). This can be observed in figure 2*a* for the smooth wall case, which at $Re = 280,000$ results in a phase lag of about 24° degrees, in good agreement with the fit of Mier *et al.* (2021) and the literature results they surveyed (figure 2*b*). For the rough-wall cases at $Re = 280,000$, the shift is again a phase lead, about 12° for disks and ellipses and 30° for pyramids, consistently with the expectation that roughness promotes turbulence and transitional features disappears at lower Reynolds numbers. The roughness size seems to play a role in the phase shift as observed for the overall waveform. Pedocchi & Garcia (2009) derived a semi-empirical formula to calculate the phase lead calibrated with literature results on sand-paper beds, and based on the oscillatory Reynolds number $Re = U_0 a/\nu$ and the ratio a/k (k is the hydraulic roughness, 2.5 times the mean sand diameter). Adapting their model to the present configuration, one estimates a phase lead of about 22° for disks and ellipses and 26° for pyramids. While the pyramid-bed case is predicted closely (13% discrepancy), the model overestimates the phase shift for the other two cases, suggesting that roughness shape beyond size may play a deeper role in the bed hydrodynamics.

Clearly, the effects of the roughness on the temporal evolution of the flow oscillation are not confined to bed, but extended across the boundary layer. For instance, several semi-empirical models have been put forward to describe the structure of the mean (ensembled-averaged) velocity field, such as the variation of the phase lead from the bed to the free-stream and the ensembled-averaged velocity profile (Nielsen, 2016; Teng *et al.*, 2022; Dunbar *et al.*, 2023*b*). Typically, following a classic dimensional argument (e.g. Jonsson, 1966), these models take as input the Reynolds number and a single size parameter to represent the bed morphology, such as the ratio a/k_s between the oscillation excursion $a = U_0/\omega$ and the customary Nikuradse's equivalent sandgrain roughness length k_s. For example, Dunbar *et al.* (2023*b*) recently developed a model to predict the velocity phase lead $\phi(z)$ with respect to the free-stream at different distances across the boundary layer. In the model, the boundary layer thickness δ_{bl} is estimated using the fit $\delta_{\mathrm{bl}}/k_s = 0.075\,(a/k_s)^{0.82}$ from the literature (van der A *et al.*, 2011), and an analogous expression is used for the bottom phase lead ϕ_0 (Humbyrd, 2012). For the present results, k_s is calculated from the mean velocity profiles and roughness function ΔU^+ during the deceleration phases of the cycle (when a log layer can be identified in viscous scaling; see e.g. Kaptein *et al.*, 2020). Model results (dashed lines) are compared against simulation results (symbols) in figure 3. The model evaluation using the empirical fit from the literature leads to an overestimation of the phase delay throughout the whole boundary layer. However, when calculations are repeated using the boundary layer thickness δ_{bl} and bot-

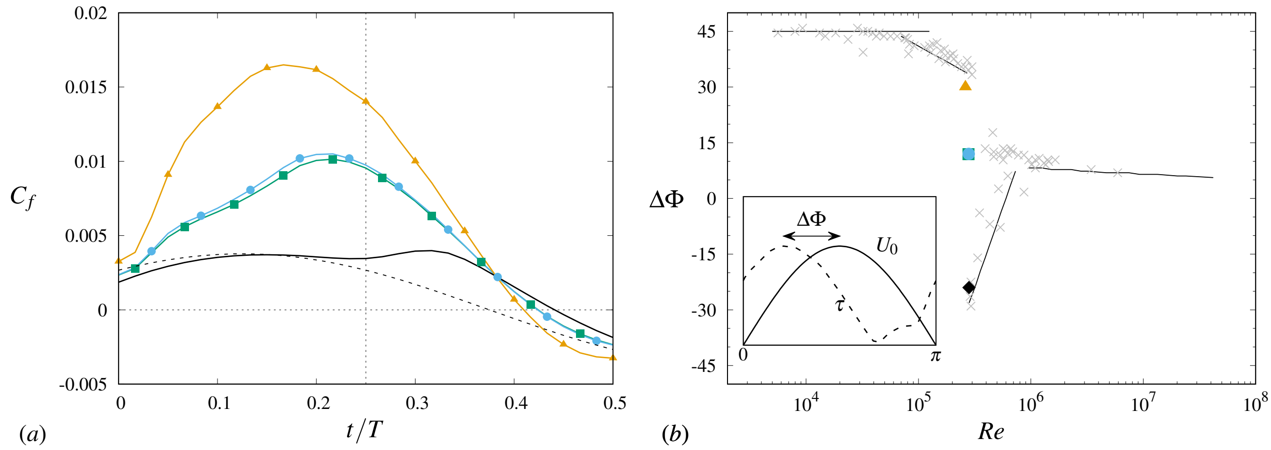

Figure 2. Bed shear stress, (a) evolution over half a cycle and (b) stress-velocity phase shift as a function of Reynolds number: ■ disks; • ellipses; ▲ pyramids. The solid line in (a), and ♦ in (b), represent the smooth wall reference at $Re = 280{,}000$, whereas the dashed line in (a) is the analytical (laminar) Stokes' solution, $C_f = 2Re^{-1/2}\sin(\omega t + \pi/4)$. The vertical dashed line in (a) denotes the peak velocity phase ($t = T/4$). Grey points in (b) are literature data reported in Mier *et al.* (2021); the lines are the analytical (laminar case) solution or semi-empirical fits from the literature. The inset in (b) shows the definition of the phase shift (positive, stress phase lead).

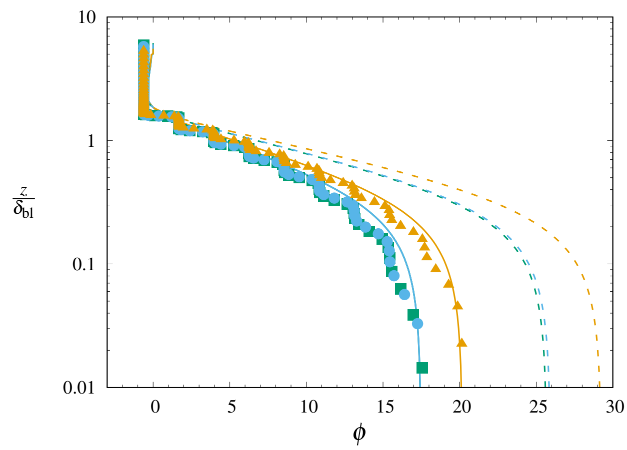

Figure 3. Phase shift across the boundary layer as a function of the normalized distance from the crest plane z/δ_{bl}. Symbols, present simulations: ■ disks; • ellipses; ▲ pyramids. Lines correspond to the model by Dunbar *et al.* (2023b) with colors corresponding symbols to denote the bed: dashed lines correspond to model calculations made with literature fits, solid lines correspond to calculations using present simulation results.

tom phase lead directly evaluated from the current direct numerical simulations, the agreement of the model with the numerical data is much improved (solid lines in figure 3). This suggests that scaling with a single "bulk" roughness size parameter, such as k_s, may not capture the full effect of the bed morphology, especially in when considering scenarios that depart from the common 'spherical-sand' type of roughness that is predominant in literature data employed for semi-empirical fits. Indeed, more geometrical bed parameters may be required for a complete scaling to capture the effect of sediment shape, angularity and even layout on the hydrodynamics.

Considering the effect on the turbulent flow field, figure 4 shows the maximum of the period-averaged turbulence intensity in the streamwise ($\overline{\langle u'u' \rangle}^{1/2}_{\max}$, figure 4$a$) and bed-normal ($\overline{\langle w'w' \rangle}^{1/2}_{\max}$, figure 4$b$) directions. The overline denotes the average over the period, and the maximum is calculated along the wall-normal direction. We note that the flucutations are computed with respect to the ensemble average (e.g., $u' = U - \langle U \rangle$) and are devoided of the dispersive component due to the bed height heterogeneity. The maximum turbulence intensities are plotted as a function of the parameter a/k_s, which is usually employed in the literature to scale rough-wall results in addition to the Reynolds number Re_δ (Sleath, 1987; Jensen *et al.*, 1989). The present results in figure 4 are compared against literature data and trends from experimental tests over beds made of relatively well rounded and uniform sand and pebbles. The comparison suggests that the streamwise component scales quite well with the literature results for the three beds considered. However, the same cannot be said for the wall-normal component in the case of the pyramid-bed, which seems an additional indication that particle shape and angularity do play a role, not entirely captured by a single parameter k_s. It appears that the large peaks in the bed made of pyramids (figure 1) affect differently the streamwise and wall-normal fluctuations than the more isotropic disks and ellipses.

In effect, even larger differences are observed when looking more in detail at the turbulence structure over the bed. Figure 5 illustrates the evolution of the ratio between the spanwise (ℓ_y) and streamwise (ℓ_x) integral length scales over half a cycle (the other half is symmetric) at a distance of $z^+ = zu_\tau/\nu = 15$

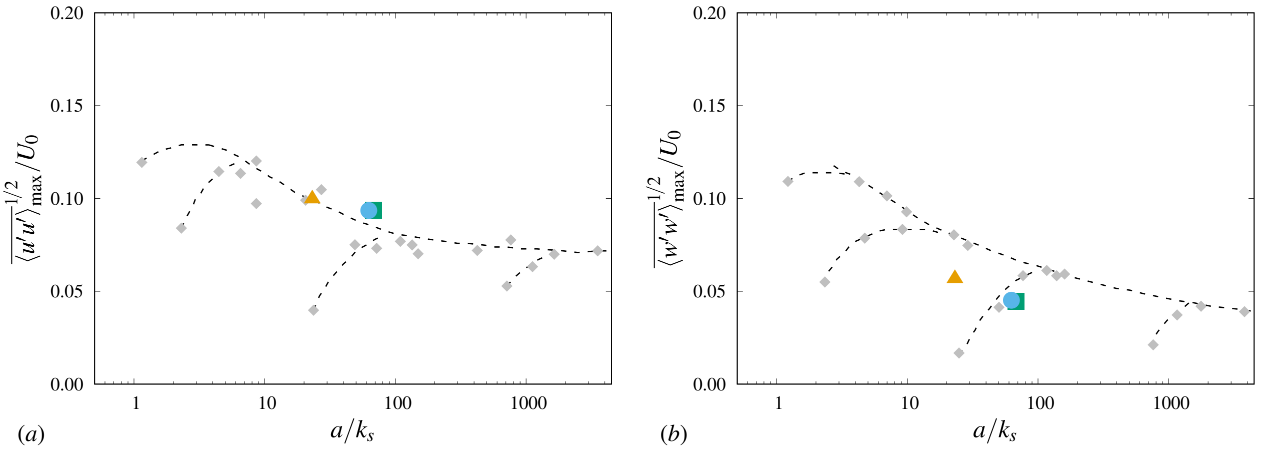

Figure 4. Maximum period-averaged rms fluctuation in the streamwise (*a*) and bed-normal (*b*) directions as a function of a/k_s: ■ disks; ● ellipses; ▲ pyramids. Grey points are literature data from Sleath (1987, 1988) and Jensen *et al.* (1989); and the lines are fits from Jensen *et al.* (1989).

(here $u_\tau = \sqrt{\tau_{\max}/\rho}$ is computed using the maximum drag value over the cycle, figure 2). The ratio of the two length scales, which is a measure of structure isotropy, has a clear dependence on the sediment shape during the acceleration phase ($0 \gtrsim t/T \gtrsim < 0.25$), even for the disks and ellipses. Discrepancies between the latter two surfaces (which have fairly similar average statistics, table 1) were not apparent looking at bulk statistics, such as the maximum turbulence intensity (figure 4), but become more noticeable in phase-dependent spatial distribution properties of near-bed turbulence. These characteristics have signifcant implications in the near-bed dynamics of sediments (e.g., erosion, transport and deposition) and nutrients, and, thus, needs to be quantified and characterized. However, as observed above for other ‘detailed’ (rather than ‘bulk’) flow statistics, it appears that a single roughness size parameter is insufficient to fully capture the complexity of flow behaviour generated by the bed roughness features.

CONCLUSIONS

Direct numerical simulations of oscillatory turbulent flows over different rough walls, modeled with the immersed boundary method, have been performed. The rough walls have been reconstructed from visualization of laboratory experiments on three beds made of different particles each, respectively disks, ellipses, and pyramids. While the immersed boundary method does not reproduce the single sediments, but rather their collective upper envolope, the walls obtained from the reconstruction enable, at least to a first approximation, to assess the hydrodynamic effect of sediment shape by comparing relatively round particles (ellipses) with very angular sediments (pyramids) and sediments with sharp edges (disks). These latter shapes are representative of seabeds in tropical areas, differently from rounded particles typical of silica sands, that make the majority of studies in the literature.

Overall the results illustrate that the sediment shape has a significant effect on the flow in the oscillatory boundary layer. Considering “bulk,” global, flow statistics such as the bed drag C_f, the roughness size alone appears to dictate the overall behavior of the surface, with disks and ellipses showing very similar temporal evolution and magnitude despite the different in the sediment grain shape. Consistently, the bed made of pyramids, which is the ‘rougher’ of the three, presents the largest departure from the smooth wall reference, highest maximum drag and increased phase-lead with the free-stream.

Nevertheless, a single roughness parameter (such as the equivalent roughness length k_s) does not seem sufficient to fully characterize the hydrodynamics over the rough bed, at least for the types of sediments considered in this study. This occurs not only on higher-order flow statistics, such as the turbulent field, but also on more fine-grained phase-dependent ensemble-averaged velocity statistics. For example, the phase lead across the boundary layer is not captured by semi-empirical models calibrated with rounded sand-paper literature results and dependent on a single roughness parameter (in this case, k_s). Rather, when the same model is adapted to replace literature fits with data directly evaluated from the simulations, the accuracy is significantly improved. While this is generally to be expected statistically, nonetheless suggests that, when considering scenarios that depart from the common ‘spherical-sand’ type of roughness predominant in the literature, more than one geometrical bed parameter is required to capture the effect of sediment shape and angularity. Similar conclusions can be made for the turbulent flow field, when moving from the turbulence intensity scaling to the details of turbulent structures. In fact, considering the ratio of the streamwise and spanwise integral length scales, substantial differences are observed even between ellipses and disks, that have similar overall roughness statistics, but induce distinct turbulent hydrodynamics over the bed. While this study has considered three beds at one single Reynolds number and future work should expand the parameter space, the results are nonetheless instructive.

REFERENCES

van der A, D. A., O’Donoghue, T., Davies, A. G. & Ribberink, J. S. 2011 Experimental study of the turbulent boundary layer in acceleration-skewed oscillatory flow. *J. Fluid Mech.* **684**, 251–283.

Arenas, I., García, E., Fu, M. K., Orlandi, P., Hultmark, M. & Leonardi, S. 2019 Comparison between super-hydrophobic, liquid infused and rough surfaces: a direct numerical simulation study. *J. Fluid Mech.* **869**, 500–525.

Batchelor, G. K. 1967 *An Introduction to Fluid Dynamics*. Cambridge, UK: Cambridge University Press.

Chan-Braun, C., García-Villalba, M. & Uhlmann, M. 2011 Force and torque acting on particles in a transitionally rough open-channel flow. *J. Fluid Mech.* **684**, 441–474.

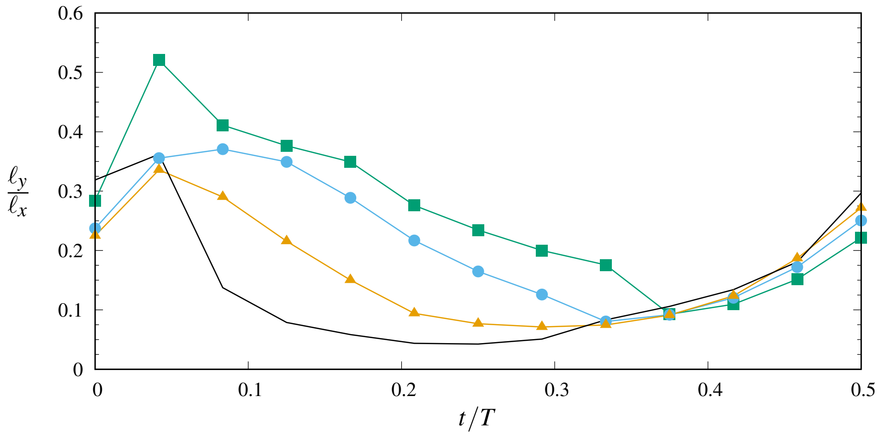

Figure 5. Evolution of the horizontal integral length scale ratio over one period: ■ disks; ● ellipses; ▲ pyramids. The solid black line is the smooth wall reference at the same *Re*.

Ciri, U., Rodríguez-Abudo, S. & Leonardi, S. 2024 Comparison between shear-driven and pressure-driven oscillatory flows over ripples. *J. Fluid Mech.* **998**, A42.

Ciri, U., Tubije, J. M. B., Guzmán-Hernandez, M. A., Rodríguez-Abudo, S. & Leonardi, S. 2023 Direct numerical simulations of oscillatory boundary layers over rough walls. *Intl. J. Heat Fluid Flow* **103**, 109170.

Dixen, M., Hatipoglu, F., Sumer, B. M. & Fredsøe, J. 2008 Wave boundary layer over a stone-covered bed. *Coastal Engng.* **55** (1), 1–20.

Dunbar, D., van der A, D. A., Scandura, P. & O'Donoghue, T. 2023*a* An experimental and numerical study of turbulent oscillatory flow over an irregular rough wall. *J. Fluid Mech.* **955**, A33.

Dunbar, D., O'Donoghue, T., Scandura, P. *et al.* 2023*b* An empirical model for velocity in rough turbulent oscillatory boundary layers. *Coastal Engng.* **179**, 104242.

Fornarelli, F. & Vittori, G. 2009 Oscillatory boundary layer close to a rough wall. *Eur. J. Mech.-B/Fluids* **28** (2), 283–295.

Fytanidis, D. K., García, M. H. & Fischer, P. F. 2021 Mean flow structure and velocity–bed shear stress maxima phase difference in smooth wall, transitionally turbulent oscillatory boundary layers: direct numerical simulations. *J. Fluid Mech.* **928**.

Ghodke, C. D. & Apte, S. V. 2016 DNS study of particle-bed–turbulence interactions in an oscillatory wall-bounded flow. *J. Fluid Mech.* **792**, 232–251.

Ghodke, C. D. & Apte, S. V. 2018*a* Roughness effects on the second-order turbulence statistics in oscillatory flows. *Comp. Fluids* **162**, 160–170.

Ghodke, C. D. & Apte, S. V. 2018*b* Spatio–temporal analysis of hydrodynamic forces on the particle bed in an oscillatory flow environment. *J. Fluid Mech.* **841**, 167–202.

Humbyrd, C. J. 2012 Turbulent combined wave-current boundary layer model for application in coastal waters. PhD thesis, Massachusetts Institute of Technology.

Hussain, A. K. M. F. & Reynolds, W. C. 1970 The mechanics of an organized wave in turbulent shear flow. *J. Fluid Mech.* **41** (2), 241–258.

Jensen, B. L., Sumer, B. M. & Fredsøe, J. 1989 Turbulent oscillatory boundary layers at high Reynolds numbers. *J. Fluid Mech.* **206**, 265–297.

Jonsson, I. G. 1966 Wave boundary layers and friction factors. In *Coastal Engineering Proceedings*, chap. 10, pp. 127–148. New York, NY: American Society of Civil Engineers.

Jonsson, I. G. & Carlsen, N. A. 1976 Experimental and theoretical investigations in an oscillatory turbulent boundary layer. *J. Hydraul. Res.* **14** (1), 45–60.

Kaptein, S. J., Duran-Matute, M., Roman, F., Armenio, V. & Clercx, H. J. 2020 Existence and properties of the logarithmic layer in oscillating flows. *J. Hydraul. Res.* **58** (4), 687–700.

Keiller, D. C. & Sleath, J. F. A. 1976 Velocity measurements close to a rough plate oscillating in its own plane. *J. Fluid Mech.* **73** (4), 673–691.

Mazzuoli, M. & Uhlmann, M. 2017 Direct numerical simulation of open-channel flow over a fully rough wall at moderate relative submergence. *J. Fluid Mech.* **824**, 722–765.

Mazzuoli, M. & Vittori, G. 2016 Transition to turbulence in an oscillatory flow over a rough wall. *J. Fluid Mech.* **792**, 67–97.

Mier, J. M., Fytanidis, D. K. & García, M. H. 2021 Mean flow structure and velocity–bed shear stress maxima phase difference in smooth wall, transitionally turbulent oscillatory boundary layers: experimental observations. *J. Fluid Mech.* **922**.

Nielsen, P. 2016 1DV structure of turbulent wave boundary layers. *Coastal Engng.* **112**, 1–8.

Orlandi, P. 2000 *Fluid Flow Phenomena: a numerical toolkit*. Dordrecht, the Netherlands: Kluwer Academic Publishers.

Orlandi, P. & Leonardi, S. 2006 DNS of turbulent channel flows with two-and three-dimensional roughness. *J. Turbul.* (7), N73.

O'Donoghue, T., Davies, A., Bhawanin, M. & van der A, D. 2021 Measurement and prediction of bottom boundary layer hydrodynamics under modulated oscillatory flows. *Coastal Engng.* **169**, 103954.

Pedocchi, F. & Garcia, M. H. 2009 Friction coefficient for oscillatory flow: the rough–smooth turbulent transition. *J. Hydraul. Res.* **47** (4), 438–444.

Sleath, J. F. A. 1987 Turbulent oscillatory flow over rough beds. *J. Fluid Mech.* **182**, 369–409.

Sleath, J. F. A. 1988 Transition in oscillatory flow over rough beds. *J. Waterway Port C.-ASCE* **114** (1), 18–33.

Teng, Y., Lu, L., Cheng, L., Tong, F. & Tang, G. 2022 A modified defect function for wave boundary layers. *Coastal Engng.* **171**, 104050.

Vargas-Martinez, J. C. & Rodríguez-Abudo, S. 2024 Simultaneous velocity and concentration measurements over a rippled boundary subjected to oscillating fluid forcing. *Exp. Fluids* **65** (7), 1–12.